Ceramics International 46 (2020) 15342–15356

Contents lists available at ScienceDirect

Ceramics International

journal homepage: www.elsevier.com/locate/ceramint

Synthesis and microstructural evolution in ternary metalloceramic Ti_3SiC_2 consolidated via the Maxthal 312 powder route

Carl Magnus[a,*], Tom Galvin[b], Le Ma[a], Ali Mostaed[c], William M. Rainforth[a]

[a] The Henry Royce Institute and Department of Materials Science and Engineering, The University of Sheffield, Sir Robert Hadfield Building, Sheffield, S1 3JD, UK
[b] M&I Materials Ltd, Hibernia Way, Trafford Park, Manchester, M32 0ZD, UK
[c] Department of Materials, University of Oxford, 16 Parks Road, Oxford, OX1 3PH, UK

ARTICLE INFO

Keywords:
Ti_3SiC_2
Metalloceramic
Spark plasma sintering
Reaction mechanism
Microstructure

ABSTRACT

A bulk specimen containing Ti_3SiC_2, $TiSi_2$ and TiC was prepared through an in situ spark plasma sintering/solid-liquid reaction powder metallurgy method using the Maxthal 312 (nominally-Ti_3SiC_2) powder as a starting material. The reaction mechanism, phase constituents and evolution of the microstructure were systematically investigated by X-ray diffraction (XRD), optical microscopy, scanning electron microscopy (SEM) equipped with energy dispersive spectroscopy (EDS) system, transmission electron microscopy (TEM), Raman spectroscopy, differential scanning calorimetry (DSC) and Vickers microhardness testing. Phase analysis and microstructural characterization revealed that the bulk sample contained binary ancillary phases, possibly due to Si evaporation and/or carburization. The deformed microstructure around the indents revealed evidence of plasticity, intrinsic lubricity and toughening. The Microstructural and orientation relationships between the phases contained in the bulk sample are reported.

1. Introduction

Upon the discovery that the ternary metalloceramic compounds with $M_{n+1}AX_n$ (MAX) chemistry (where n = 1–5, M is an early transition metal, A is an A-group and X is C or N) possess an unusual and sometimes unique set of properties, they have been extensively studied [1–3]. The fact that the 2-D materials known as MXenes, which cannot be synthesized directly due to their thermodynamic metastability [4–6] can be synthesized directly from 3-D MAX phases (by taking advantage of the significant difference in strength between the metallic M–A bonding and covalent M–X bonding, which aids in selectively etching out the A-layer to form two-dimensional MXenes) have further attracted extensive interest in MAX phases [7]. Well over 100 MAX phases have now been successfully synthesized, and in some cases 'hybrid' MAX phases, consisting of a partial substitution of the M or A elements have also been found to be stable [1–3,8].

MAX phases typically exhibit properties between those of metals and conventional ceramics [1]. They have high electrical and thermal conductivity while also showing creep resistance, high temperature strength, and good resistance to thermal shock and oxidation [9]. They are stiff (Ti_3SiC_2 has around three times the stiffness of titanium with a comparable density [10]) and relatively soft compared to their binary carbide equivalents, so much so that MAX phases are easily machinable with common metalworking tools such as hacksaws or lathes [11]. Due to their layered structure, MAX phases are surprisingly damage tolerant; the layers slide, kink and delaminate to absorb the deformation, causing local hardening at the damage site [12–14]. Currently, MAX phases find applications as furnace tubes and high temperature burner nozzles, as well as electric furnace elements [10]. They have been proposed for use as latex glove formers [10], and, due to some favourable radiation tolerance studies [15–18] MAX phases are also being considered as a potential material for use within current and future designs of nuclear fission reactor [19,20]. Their layered nature and self-lubricating properties make them a candidate for bearings and other sliding applications [21–24].

Titanium silicon carbide (Ti_3SiC_2) is a member of the $M_{n+1}AX_n$ layered compound belonging to the $Ti_{n+1}SiC_n$ system. It is the most stable ternary phase in Ti–Si–C ternary phase system and crystallizes in the space group of $P6_3/mmc$ [25]. However, its formation is compromised by more stable binary phases (TiC, SiC and $TiSi_2$) due to its narrow formation region in the Ti–Si–C Phase diagram [25]. The bonding in Ti_3SiC_2 is anisotropic as well as metallic-covalent-ionic in nature [26]. This unusual bonding characteristics and special crystal structure render the MAX phases with unique properties [27]. Ti_3SiC_2, just like other members of the MAX phases does not melt but instead decomposes into its respective binary phases via the dissociation of Si at

* Corresponding author.
E-mail address: mcarl2@sheffield.ac.uk (C. Magnus).

https://doi.org/10.1016/j.ceramint.2020.03.078
Received 10 December 2019; Received in revised form 14 February 2020; Accepted 7 March 2020
Available online 08 March 2020

specific temperature in various atmosphere [28]. It is reported to be stable under vacuum or argon atmosphere up to 1600 °C [29]. All these exciting properties makes it a promising next generation material suitable in a range of structural applications as a monolithic phase and/or composite [30]. Some authors have reported that the composite form, Ti_3SiC_2–TiC and Ti_3SiC_2–SiC for example, possesses superior mechanical properties than monolithic Ti_3SiC_2 [31,32].

There are several synthesis routes to produce Ti_3SiC_2. Hot Pressing/Hot Isostatic Pressing (HIP) [33,34], as used by Barsoum and El-Raghy in their initial paper on Ti_3SiC_2 [35], and Spark Plasma Sintering

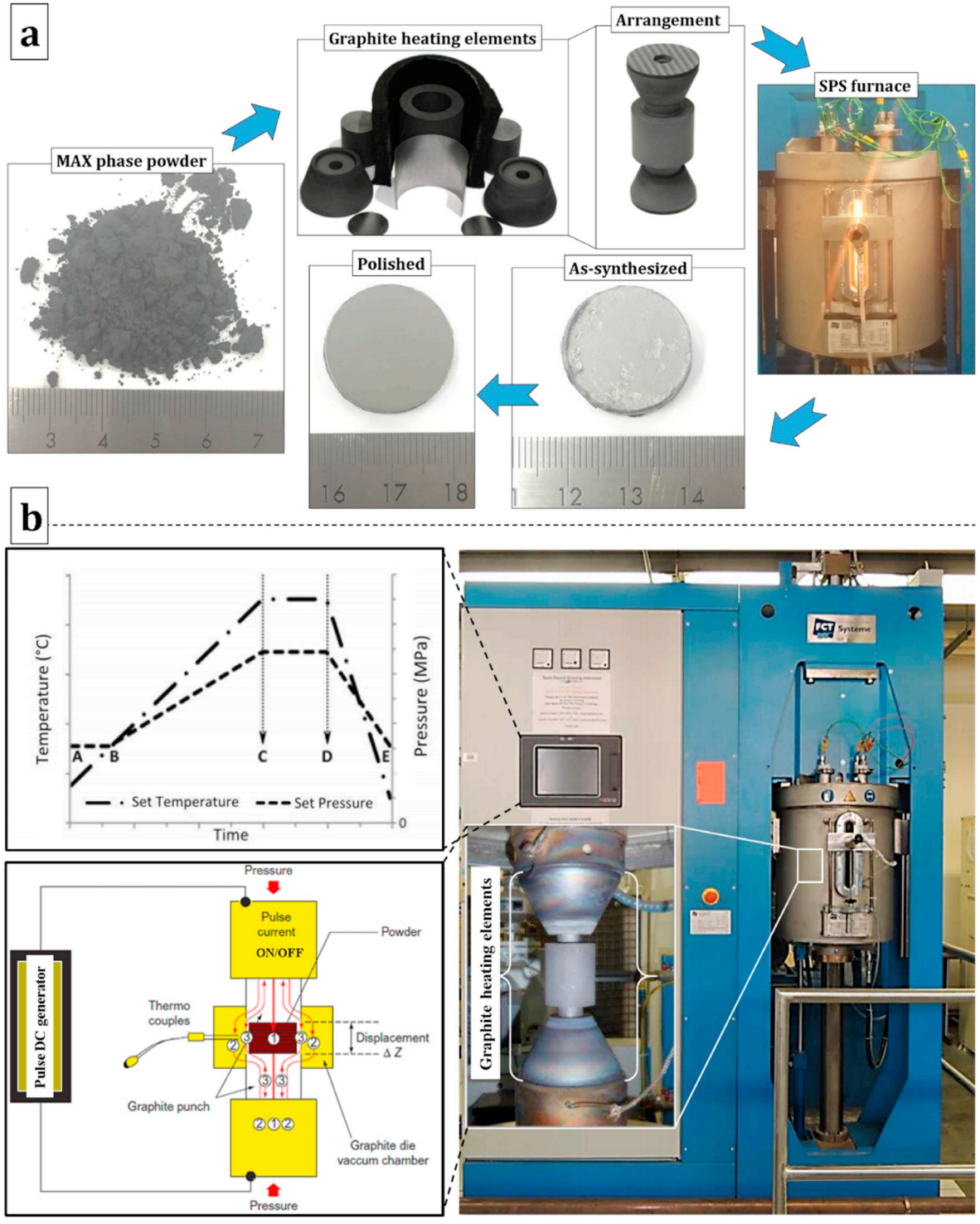

Fig. 1. (a) Punch-powder-die assembly and (b) SPS furnace unit and associated sintering parameters.

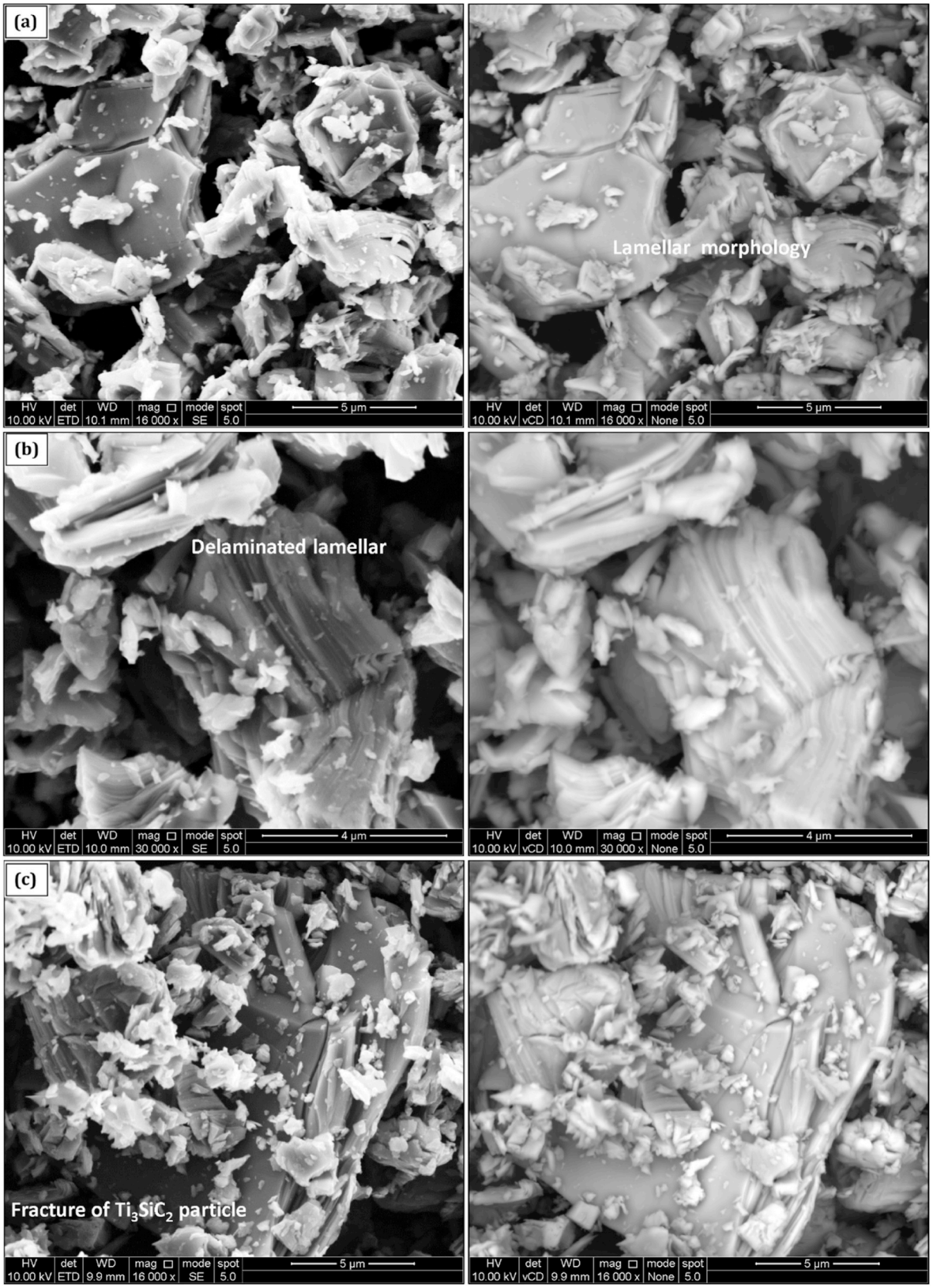

Fig. 2. SEM (SE–BSE) micrographs showing the morphology of the as-received Maxthal 312 (nominally-Ti_3SiC_2) powder.

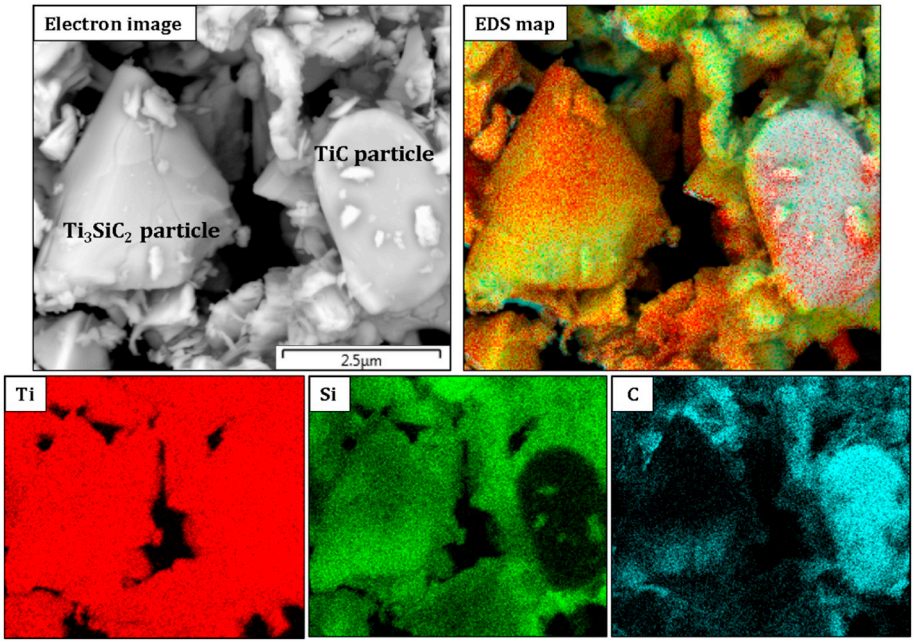

Fig. 3. EDS elemental mapping of the as-received Maxthal 312 (nominally-Ti_3SiC_2) prealloyed powder.

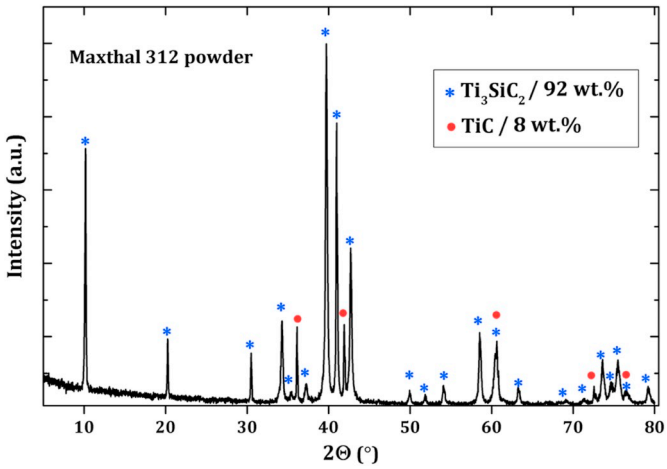

Fig. 4. XRD pattern of the as-received Maxthal 312 (nominally-Ti_3SiC_2) powder.

[36–39] are common methods, which produce bulk samples. Self-propagating High-temperature Synthesis (SHS) is also employed to produce a low density product, which is commonly crushed to a powder for secondary densification [40–43]. Ancillary phases such as TiC, $TiSi_2$ and SiC are often reported to coexist with Ti_3SiC_2 during synthesis [24,44,45]. However, the addition of aluminium [36,46] in a controlled amount in the starting powder mixture and/or over-stoichiometric starting powder mixture containing excess silicon [47] has been shown to reduce the ancillary phases produced.

The scope of this study is to investigate the formation of Ti_3SiC_2 via the prealloyed powder route and determine the reaction mechanism and the resulting microstructural evolution. It is noteworthy that synthesizing high purity Ti_3SiC_2 is not the aim of this work but instead to further contribute to the metallurgy of Ti_3SiC_2. Spark plasma sintering (SPS) technique is a synthesis and densification sintering process with the advantage of rapid heating rate and short sintering time. Most especially, the short sintering time is advantageous in suppressing grain growth [48] and the range of controllability of sintering parameters enables tailoring of the evolved microstructure.

2. Material and methods

Pre-reacted commercially available Ti_3SiC_2 powder (Maxthal 312 (nominally-Ti_3SiC_2); particle size 2 μm, Kanthal AB, Sweden) was used as starting powder. The composition of the as-received Maxthal 312 powder were 92 wt% Ti_3SiC_2 and 8 wt% TiC, respectively. The powder was initially cold-pressed in a graphite die (Ø = 20 mm) in between two graphite punches with the inner wall of the die and surface of the punch covered with graphite paper to isolate the powder from the die and punches. The die-powder-punch assembly was then wrapped with graphite felt to minimize possible heat dissipation during the synthesis and subsequently loaded into the SPS furnace unit (HP D 25; FCT Systeme GmbH, Rauenstein, Germany) as shown in Fig. 1. The consolidation was carried out at a requisite sintering temperature of 1400 °C with a hold time of 5 min, the heating rate was 100 °C/min whilst the load (54 MPa) was applied at room temperature and removed at the end of the dwell time. During the synthesis, the chamber was maintained under vacuum (10^{-2} Pa) and the temperature was controlled by a thermocouple that measured the temperature in the interior of the graphite punch. The sintering temperature was selected based on a preliminary test which ensured the bulk composition fell within a three-phase region, as purity of the bulk sample is not the scope of this work.

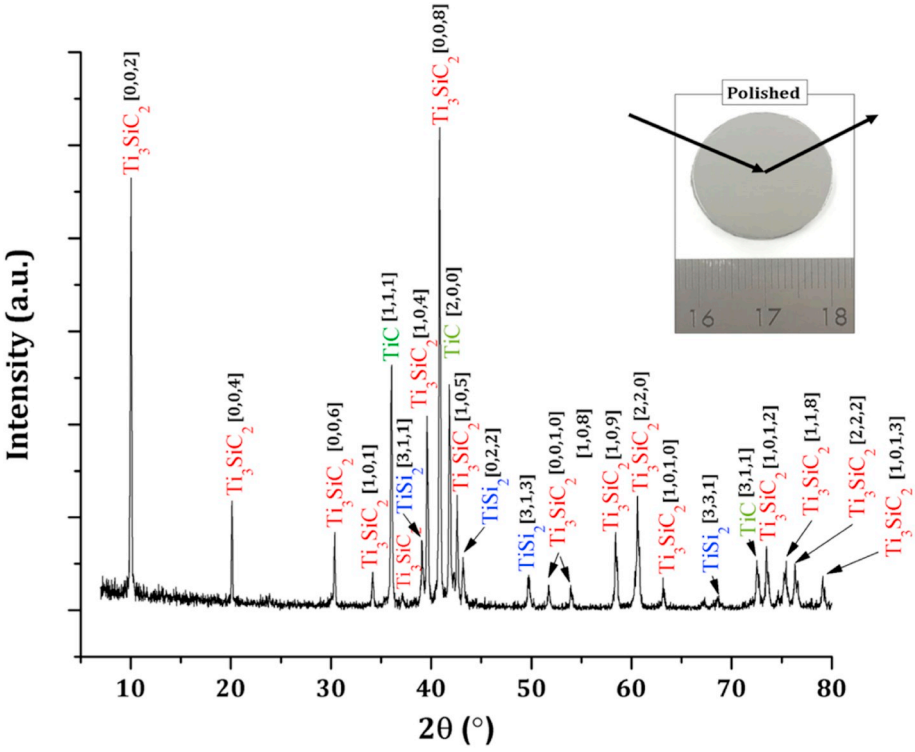

Fig. 5. XRD pattern of the synthesized sample after polishing. Inset shows the pattern was collected from the polished disc.

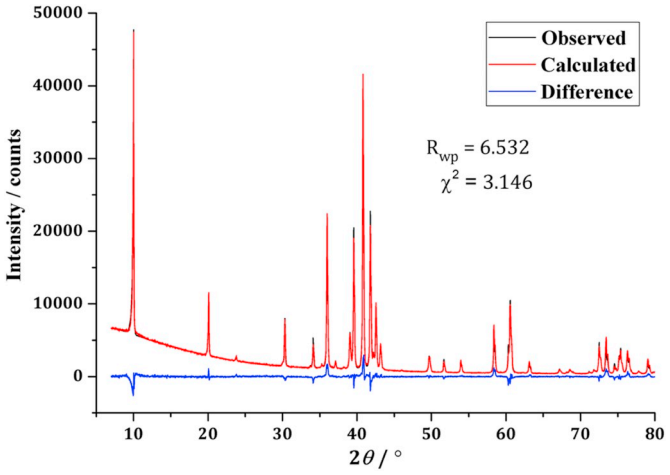

Fig. 6. Rietveld refinement of the XRD pattern of the bulk sample in 2Θ range from 5 to 80°.

2.1. Characterization

X-ray diffraction (XRD) patterns were obtained with a $\theta - 2\theta$ diffractometer (Bruker D2 Phaser, Germany) using Cu Kα radiation source in steps of 0.02° at 1 s/step. The surface layer of the as-sintered disc was removed by grinding prior to XRD analysis. Phase identification was performed using DIFFRAC EVA software suite whilst the phase quantification was obtained by Rietveld refinement (TOPAS) from the diffraction pattern collected in the 5–80° (2Θ) range using X'pert[3] diffractometer (Malvern Panalytical, UK). Microstructural evolution was investigated using scanning electron microscopy (SEM; Inspect F50, FEI The Netherlands) equipped with an EDS detector (Oxford Instruments X-Max/Aztec Nanoanalysis, UK) and transmission electron microscopy (TEM; Philips EM420/120 kV and JEOL JEM-F200/200 kV). TEM electron transparent samples from selected areas were prepared using a focused ion beam (FIB; FEI Helios NanoLab G3 UC, FEI company, The Netherlands). The Vickers hardness (HV) of bulk sample was measured using an indentation load of 19.6 N for 15 s (DuraScan G5 emcoTEST, Austria). The density of the bulk sample was measured (following mirror-like metallographic polishing down to 0.5 μm diamond paste) by the Archimedes' method in water at ambient conditions. Raman analysis was carried out ex-situ on the polished surface by employing a Si-calibrated inVia Raman spectrometer (Renishaw plc, UK) with an Ar laser (λ = 514.5 nm, laser output power 20 mW) and a 50x objective lens (spot size of 2 μm). In order to further understand the phase transformations and reaction mechanisms during synthesis, simultaneous thermal gravimetric analysis (TGA)-differential scanning calorimetry (DSC) experiment was conducted on the Maxthal 312 powder (Q600, TA Instruments) from 25 to 1500 °C in a high purity dynamic nitrogen atmosphere using Al_2O_3 crucible.

3. Results and discussion

3.1. Morphology of Maxthal 312 powder

The morphology of the as-received Maxthal 312 powder is shown in Figs. (2) and (3). Fig. 2 shows the characteristic lamellar nature of the

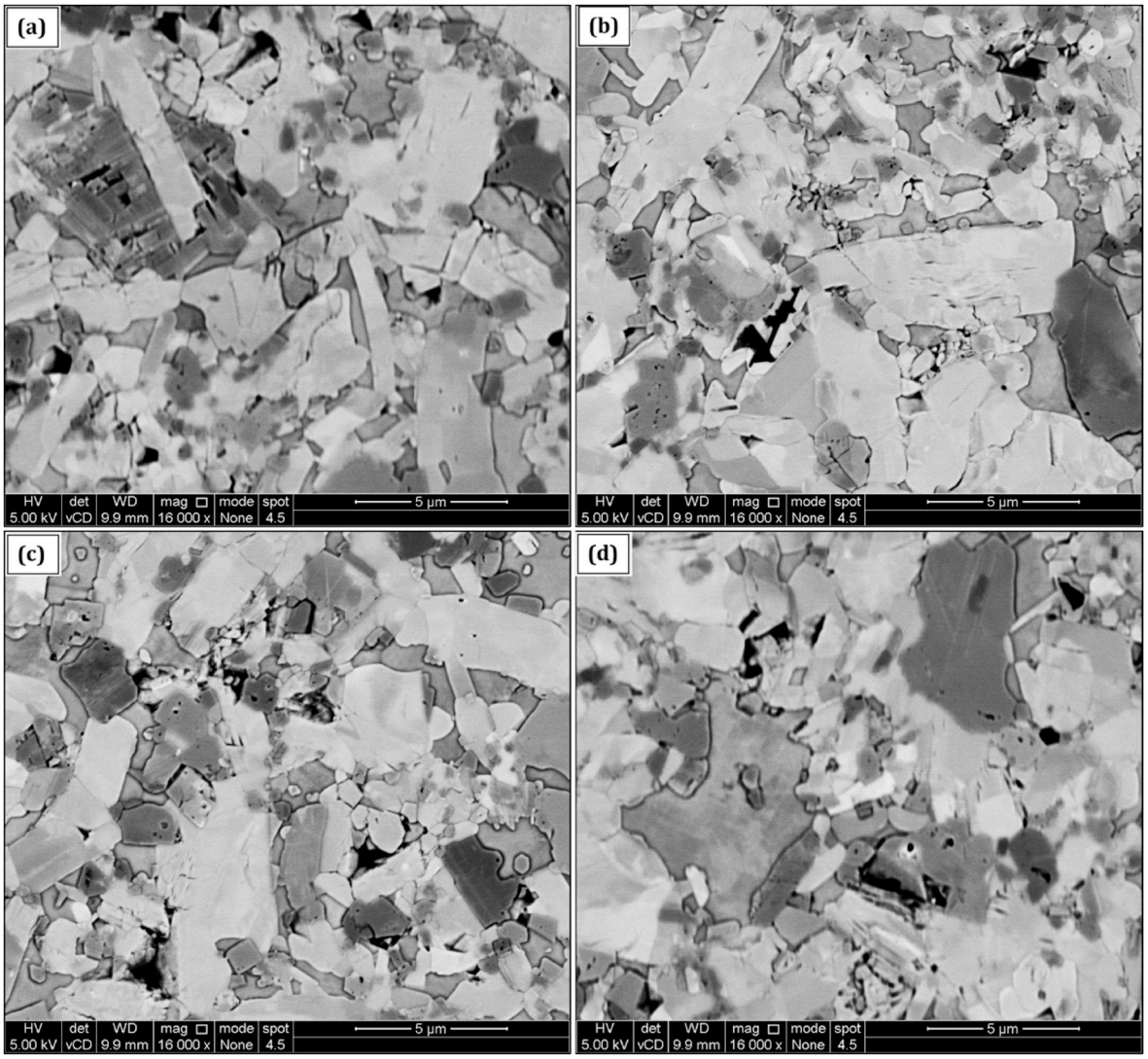

Fig. 7. Backscattered electron (BSE) images of the bulk sample produced by SPS using the Maxthal 312 powder. Note the homogenous dispersion of the in situ formed TiC in the Ti_3SiC_2 matrix.

Ti_3SiC_2 MAX phase compound, whilst Fig. 3 is an EDS elemental map which reveals the coexistence of TiC particle in the as-received pre-alloyed powder in the form of an ancillary.

3.2. Phase analysis and densification

X-ray diffractogram (XRD) from the as-received prealloyed Maxthal 312 powder confirming Ti_3SiC_2 as a major phase and some minor TiC intermetallic phase is shown in Fig. 4.

The XRD patterns showing the phase evolution of the bulk sample following spark plasma sintering of the prealloyed Maxthal 312 powder is shown in Fig. 5. It can be seen from the diffraction pattern that the bulk sample consists of three phases: Ti_3SiC_2, TiC and $TiSi_2$, respectively. In comparison to the as-received prealloyed powder X-ray diffraction pattern, additional peaks - especially two strong peaks at $2\Theta = 39^\circ$ and 43.2°, corresponding to $TiSi_2$ peaks evolved after synthesis.

Fig. 6 shows X-ray diffraction (XRD) pattern of the bulk sample ($2\Theta = 5^\circ$–80°) alongside Rietveld refinement of the pattern. The Rietveld refined parameters are $R_{wp} = 6.532$ and $\chi^2 = 3.146$, respectively. The bulk sample contained 51.8 wt% Ti_3SiC_2, 36.4 wt% TiC and 11.8 wt% $TiSi_2$, respectively. It is noteworthy that the refinement data showed strong preferred orientation in the 002 direction. This is in agreement with our earlier work which indicated preferred orientation of Ti_3SiC_2 along the pressing direction during the SPS synthesis [24]. The relative density of the polished disc was 99% upon taking into account the phase fraction of the constituent phases and their corresponding theoretical densities, respectively.

3.3. Microstructural evolution and EDS analysis

SEM backscattered electron (BSE) micrographs of the polished unetched bulk sample is shown in Fig. 7. According to the EDS analysis (Fig. 8), the bright phase is the Ti_3SiC_2 phase whilst the dark contrast is

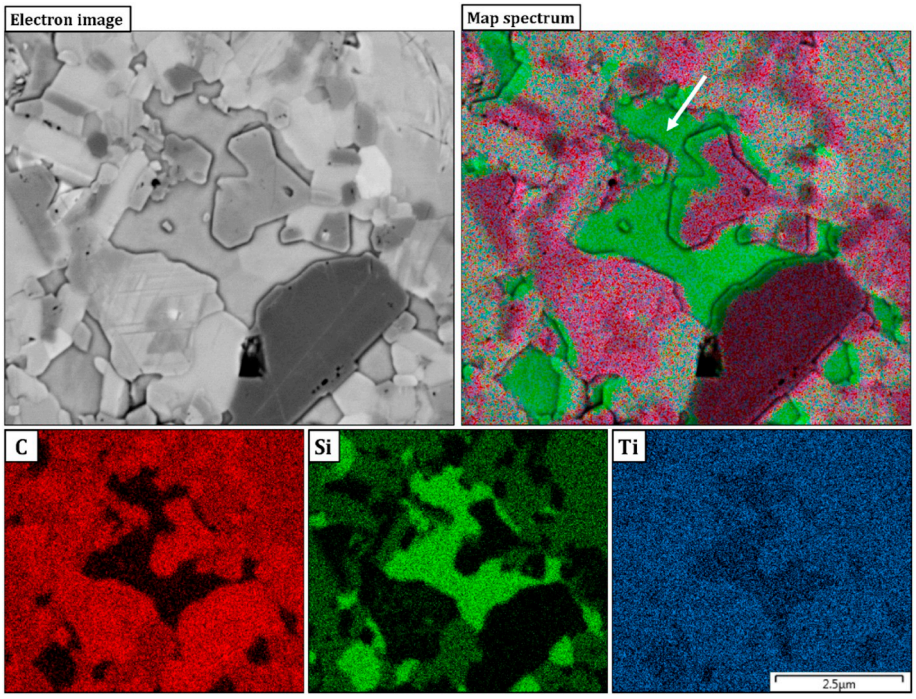

Fig. 8. Identification of particular phases in the bulk sample by EDS elemental map analysis.

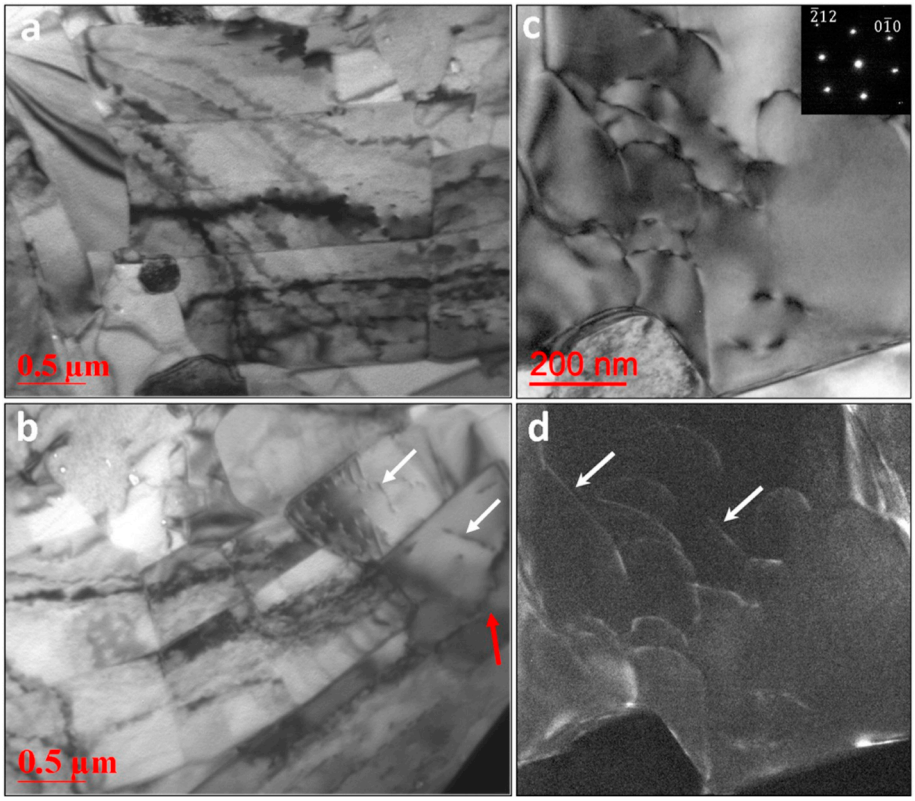

Fig. 9. (a) BF-TEM micrograph showing the plate-like morphology of the Ti_3SiC_2 grains, (b) BF-TEM micrograph showing evidence of basal plane slip (red arrow) and basal plane dislocation (white arrow), (c) BF-TEM image obtained from a Ti_3SiC_2 grain along the [101] direction and (d) DF-TEM image of dislocation shown in (c) imaging with $g = \bar{2}12$ (white arrows show edge-on basal plane dislocations). (For interpretation of the references to colour in this figure legend, the reader is referred to the Web version of this article.)

the TiC phase. Those with the medium contrast are the $TiSi_2$ liquid phase (white arrow in Fig. 8 map spectrum) - an intermediate eutectic liquid phase leading to the formation of Ti_3SiC_2 that has not been fully consumed [49]. According to Ref. [50,51], the reaction mechanism leading to the formation of Ti_3SiC_2 is a solid-liquid reaction partly due to the formation of Ti–Si eutectic liquid (eutectic temperature 1332 °C) and/or liquid Si formation (T_m of Si = 1414 °C).

Fig. 9 shows TEM images obtained from the bulk sample revealing an area containing the Ti_3SiC_2 grains. The plate-like morphology (Fig. 9(a)) typical of MAX phases can be seen alongside with evidence of basal plane dislocation (Fig. 9(b–d)) as reported elsewhere [52]. Basal plane dislocations play a key role during room-temperature

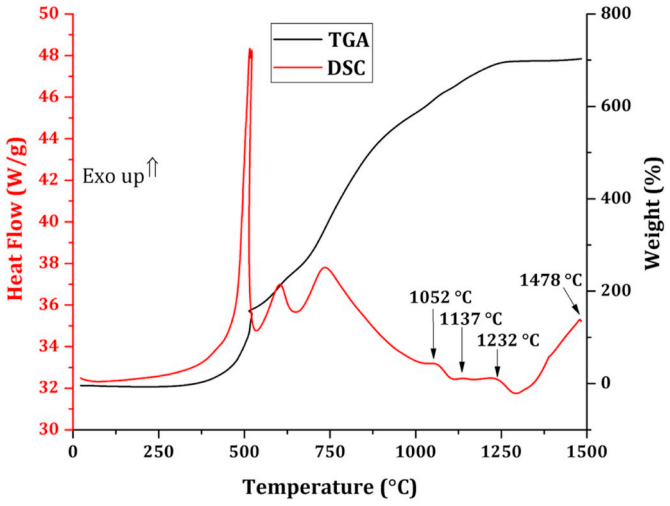

Fig. 10. Typical simultaneous thermogram of TGA/DSC of a Maxthal 312 (nominally-Ti_3SiC_2) powder.

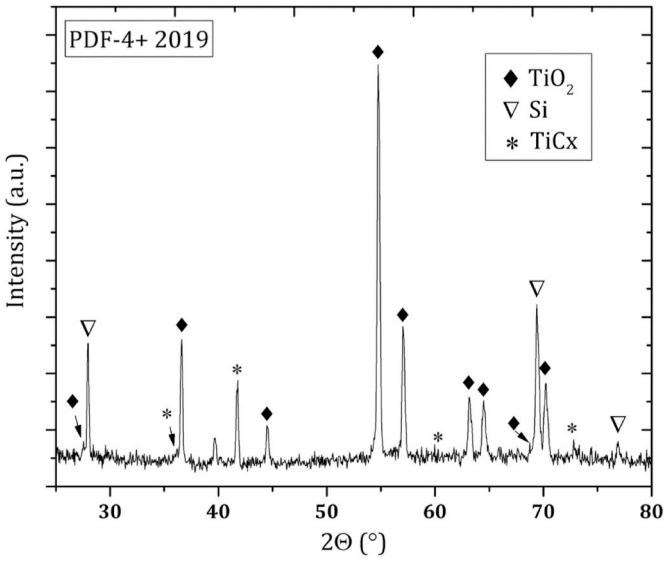

Fig. 12. X-ray (XRD) diffraction pattern of the decomposed powder after TGA/DSC thermal analysis.

deformation of MAX phases as they possess fewer than five slip systems needed for polycrystalline ductility [52,53]. The steps along the grain boundary (red arrow in Fig. 9(b)) is an evidence of slip along the basal planes [10].

3.4. Thermal behaviour of the Maxthal 312 powder

Fig. 10 shows the simultaneous DSC/TGA thermogram recorded during the heating of the Maxthal 312 powder at 20 °C/min from 40 to 1500 °C in flowing Ni. Exothermic peaks (518, 602 and 735 °C) corresponding to anatase and/or rutile TiO_2 layers were detected up to 900 °C. The observed mass increase in this temperature range is linked to the oxidation of titanium in agreement with a previous report [54]. The DSC curve further exhibited three broad overlapped exothermic peaks (1052, 1137 and 1232 °C) as the temperature is further increased. The temperature range of these exothermic peaks when compared to the SEM-EDS analysis revealing the phases in the bulk sample sintered to 1250 °C (Fig. 11), we can reasonable conclude that these peaks

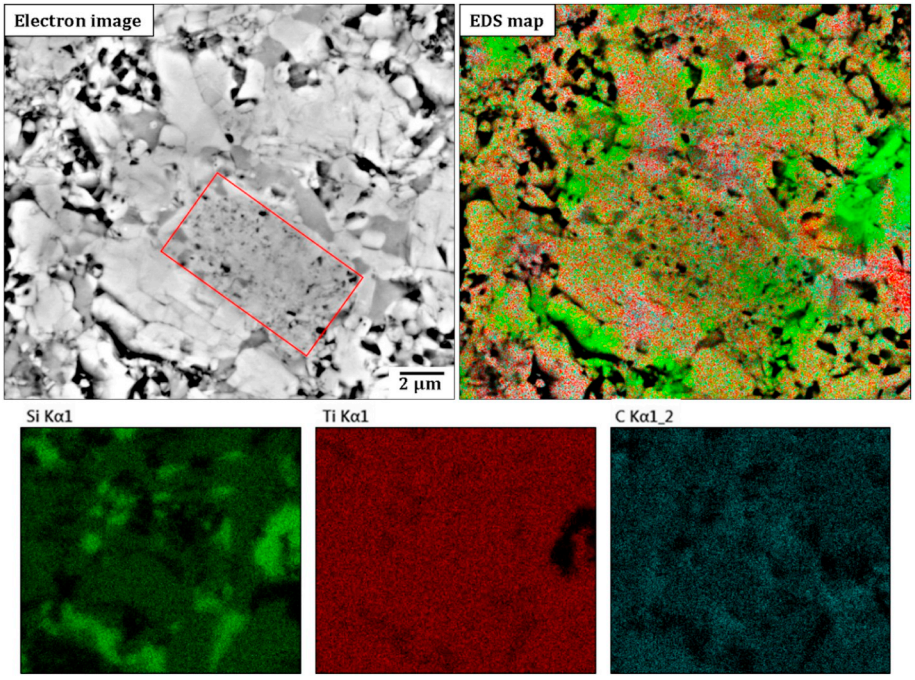

Fig. 11. EDS elemental map showing the evolution of phases in the bulk sample synthesized by SPS to 1250 °C. The highlighted section in the electron image (red rectangle) shows the growth of the Ti_3SiC_2 grains. (For interpretation of the references to colour in this figure legend, the reader is referred to the Web version of this article.)

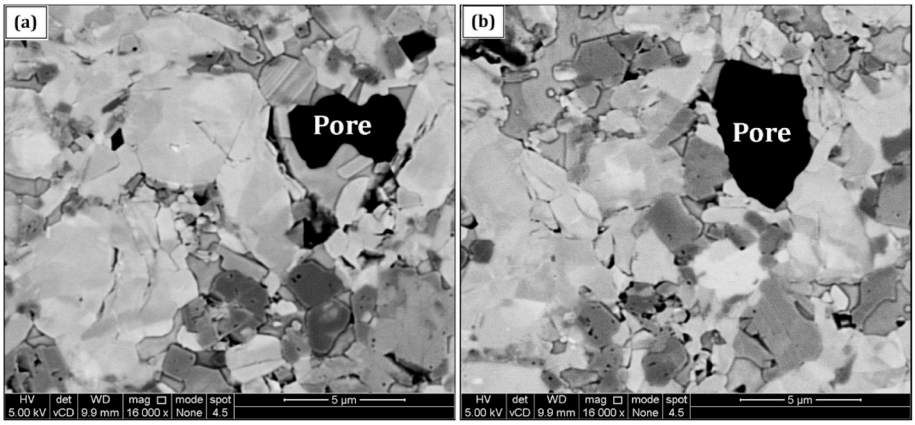

Fig. 13. Pore formation in Ti_3SiC_2 matrix owing to deintercalation of Si under high vacuum pressure.

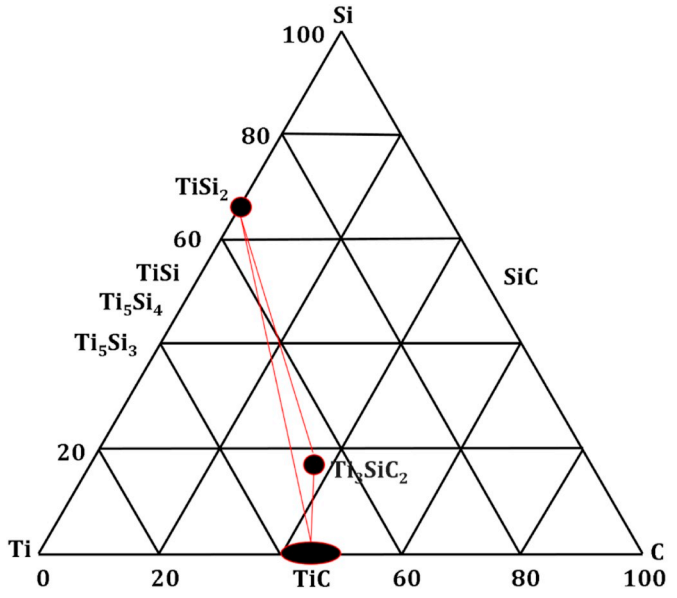

Fig. 14. Compositional diagram in the Ti–Si–C system. The three phases of interest in this work are highlighted using a triangle.

corresponds to the evolution of $TiSi_2$ and Ti_3SiC_2 phases. This is particularly true as the Ti–Si eutectic liquid will provide a direct route for the formation of Ti_3SiC_2 once the pre-existing TiC particles reacts with the Ti–Si liquid phase as proposed by Sato et al. [55] and Zhang et al. [56]. This conclusion is also in agreement with the thermogravimetric results obtained by Kero et al. [49,57], as well as observations in this work revealing the growth of Ti_3SiC_2 takes place within the Ti–Si liquid phase (electron image in Fig. 11). The last exothermic peak at 1478 °C may be attributed to TiC_x formation due to Si evaporation induced Ti_3SiC_2 decomposition as the temperature exceeds the melting point of Si (1414 °C). Fig. 12 shows the XRD pattern obtained from the decomposed Maxthal 312 powder following the thermogravimetric analysis. The phases in the decomposed powder (i.e., TiC_x, TiO_2 and Si) are in good agreement with the exothermic peaks during the thermal analysis.

3.5. Pore formation in Ti_3SiC_2

The pores formed during the synthesis of Ti_3SiC_2 such as those shown in Fig. 13 are derived from the following aspects: the original particle gap; interstitial pores left during the pressing procedure; lack of densification degree; generation of new phase in the sintering process; Si deintercalation linked to the high vacuum pressure during the SPS and/or vapourization during high temperature sintering (i.e., above the melting point of Si). The high vacuum pressure (about 10^{-3}Pa) during the SPS coupled with the high vapour pressure of silicon may have led to decomposition of Ti_3SiC_2 thus promoting pore formation via the outward diffusion of Si from the Ti_3SiC_2 grains. This is supported by observation reported elsewhere [58,59] and the hypothetical deintercalation reaction leading to pore formation given as follows [60]:

$$Ti_3SiC_2 \rightarrow 3TiC_{X=0.67} + Si(vap.)$$

This proposed loss of Si by deintercalation even at sintering temperature below the melting point of silicon (T_m = 1414 °C) contributes significantly to the loss of purity in the synthesized sample during the SPS. Investigators have often compensated for the loss of Si during vacuum sintering by silicon over-stoichiometry [47,61–63] (that is, deviation from 3:1:2 stoichiometric ratio for Ti:Si:C) in the starting mixtures to increase the conversion into Ti_3SiC_2. Another method involves the systematic addition of small amount Al in the starting powder mixture [64–66]. The increase in purity with aluminium addition is as follows: as aluminium has a relatively low melting point (660 °C), molten Al will promote the diffusion of both Ti and Si atoms thus expediting the formation of Ti_3SiC_2 via solid-liquid reaction at low temperature [67]; molten Al also acts as a deoxidation agent which promotes the synthesis of Ti_3SiC_2 [65]. It is worth mentioning that excessive Al may dilute the reactants or react with Ti to form Ti_3Al, thus compromising the phase-purity of Ti_3SiC_2.

On the other hand, pore formation may also result from possible carbon uptake from the graphite tooling (graphite paper/die/punch set-up) and its subsequent reaction with Ti_3SiC_2 which will result in bulk compositional shift into a three-phase Ti_3SiC_2–TiC–$TiSi_2$ compositional triangle (Fig. 14) following the decomposition reaction thus [68]:

$$2Ti_3SiC_2 + C \rightarrow 5TiC_X + TiSi_2$$

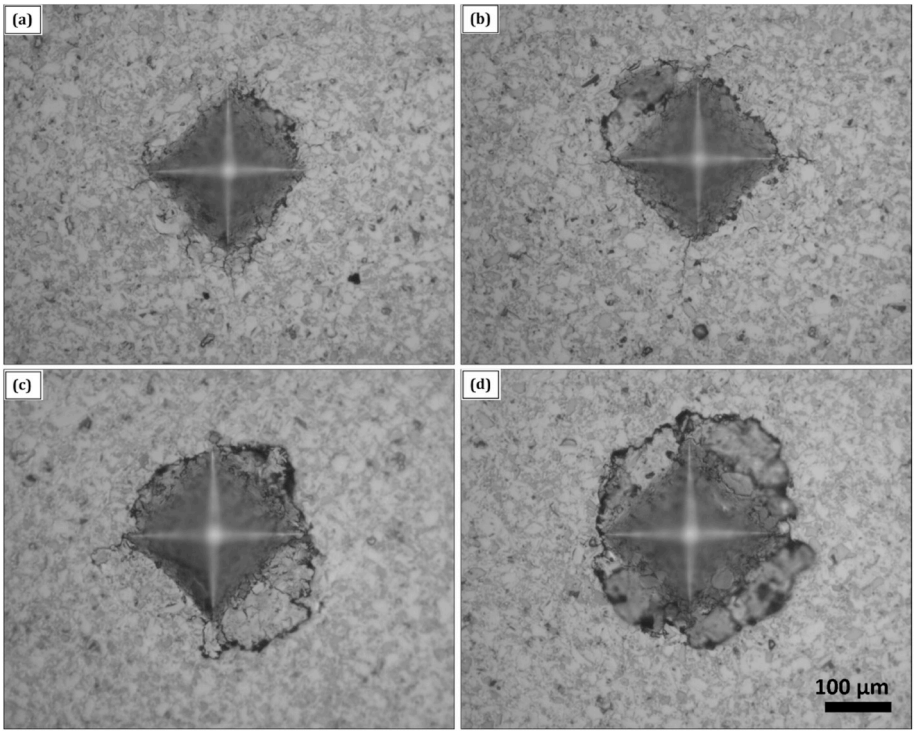

Fig. 15. Optical micrographs showing anisotropic deformation morphology following Vickers indentation.

3.6. Vickers-induced deformation microstructure

Vickers microhardness measured from the polished surface of the SPSed disc was ~5.8 GPa. This value is somewhat higher as compared to the intrinsic hardness of Ti_3SiC_2 reported to be about 4 GPa [12]. The higher hardness as compared to monolithic phase Ti_3SiC_2 may be associated to the finer microstructure introduced by SPS [61] as well as the presence of TiC ancillary in the synthesized sample. Optical micrographs (Fig. 15) obtained from the indents showed no sign of lateral cracks emanating from the indention diagonals as extensive grain pileups around the indents was operative. The ability of Ti_3SiC_2 to contain damage in limited area around the indents is a signature property of the damage tolerance capability reported in MAX phases [12,13,69,70]. Nonetheless, the extent of grain pileup – a microscale deformation mechanism owing to room-temperature plasticity [12] – varied as shown in Fig. 15(a–c) using the same indentation load. According Li et al. [71] asymmetry in the damage zone around indentation is linked to the anisotropic behaviour of Ti_3SiC_2. This is because favourably oriented grains parallel to the surface will deform by the glide of basal plane dislocations [72] to bring about grain push-outs in the vicinity of the indentation once the compressive stresses are released [12,71].

Fig. 16(a) shows the SEM micrographs obtained from the damage zones around the indentation prints on the bulk sample. No indentation-induced cracks were observed around the indentation diagonals as microdamage appears to be confined in the immediate vicinity of the indents - indicating that Ti_3SiC_2 is damage tolerant. However, the morphology of the piled grains around the indent further revealed evidence of additional micro-scale deformation mechanisms as shown in Fig. 16(b–d). The energy of an advancing crack appeared to have been consumed due to the plate-like nature of the Ti_3SiC_2 grains leading to diffuse microcracking as shown in Fig. 16(b). In addition to crack deflection, other micro-scale plasticity events such as, grain pull-out and delamination (Fig. 16(c)); grain buckling and cavitation (Fig. 16(d)) further render Ti_3SiC_2 damage tolerant [12,13]. It is noteworthy that the observed cavitation following indentation induced deformation is due to the lack of five independent slip systems needed for polycrystalline ductility in MAX phases [72,73].

An intriguing observation during the indentation is the evolution of amorphous-carbon films as shown by EDS elemental map analysis (Fig. 17) and Raman spectroscopy (Fig. 18). The evolution of amorphous carbon layer [74,75] following indentation scratch, as well as rutile phase of TiO_2 tribofilm [76] further highlights the intrinsic lubricity of Ti_3SiC_2 as reported elsewhere during tribological studies [21] and machining with cutting tools [9].

In order to clarify that the amorphous carbon films are indeed indentation-induced and not as a result of carburization from the graphite tooling employed during the SPS even though the surface of the bulk sample was polished down to 0.5 µm diamond paste, Raman spectrum was further collected from the as-synthesized surface (Fig. 19) and polished surface (Fig. 20) for validation. For the as-synthesized surface, Raman spectrum collected from the carburized surface corresponded to vibration mode of crystalline graphite [75]. The D/G intensity ratio (I_D/I_G) used as a graphitization index to monitor the deviation from the crystallinity further differentiates the graphitized layer to the amorphous carbon layer [75]. On the other hand, Raman spectrum collected

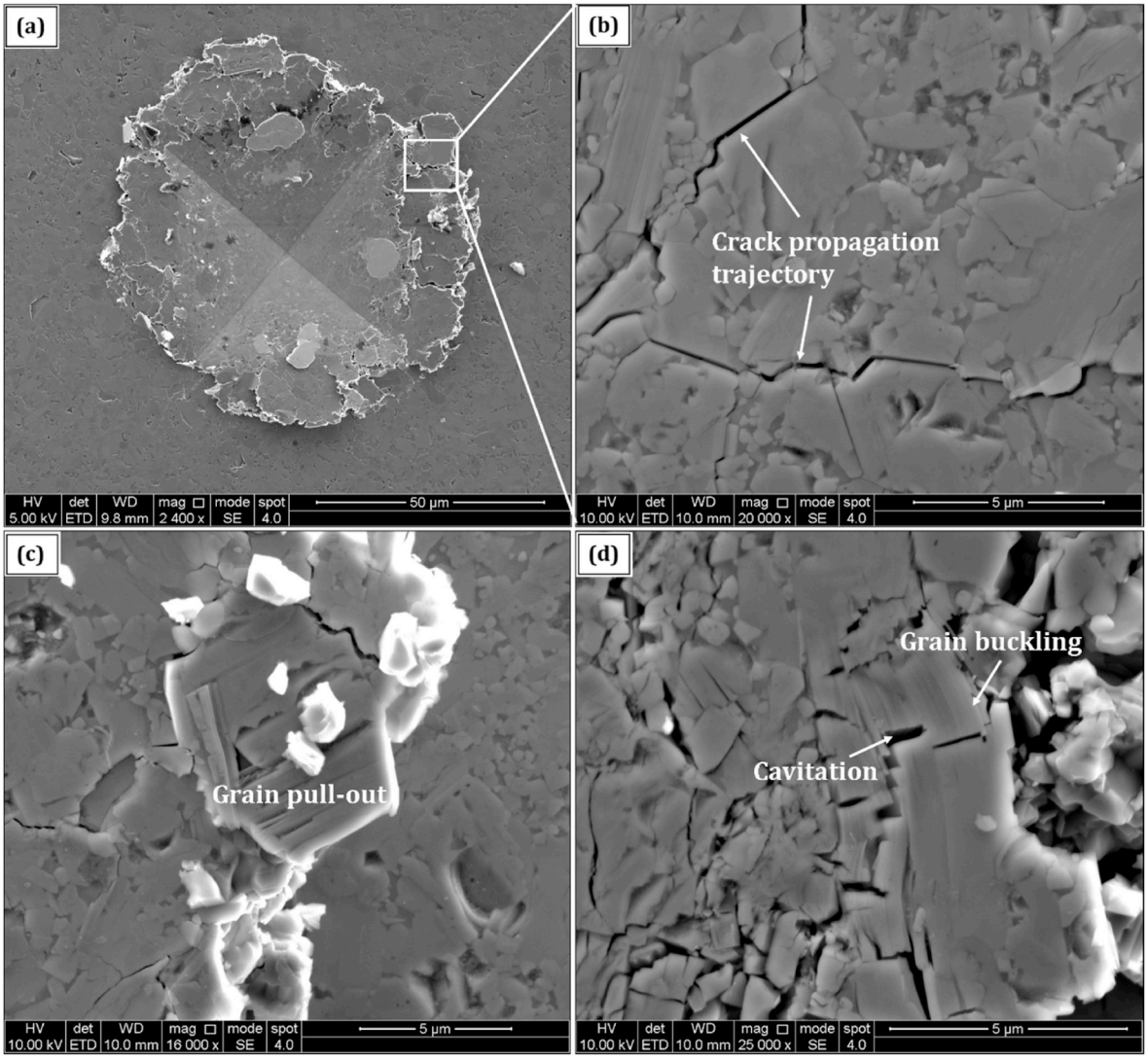

Fig. 16. (a) Scanning electron (SEM) micrographs revealing the morphology around the indent, (b) diffuse microcracking and (c–d) deformation micro-mechanisms in Ti_3SiC_2.

from the polished surface revealed vibrational modes corresponding to essentially Ti_3SiC_2 [77]. No evidence of non-stoichiometric TiC_X which possesses a Raman active mode which might have formed on the surface due to carburization was detected.

4. Microstructural and orientation relationship

An area from the bulk sample analysed by STEM-EDS is shown in Fig. 21(a–e). The EDS data confirmed the presence of all the three phases i.e. Ti_3SiC_2, TiC and $TiSi_2$. The Ti_3SiC_2 phase typically appears as elongated plate-like grains. The TiC and $TiSi_2$ phases are essentially defect-free, also, no cracking were observed at the Ti_3SiC_2–TiC interface due to coefficient of thermal expansion (CTE) mismatch between the two phases as reported elsewhere [78]. The lowest interfacial energy between TiC and Ti_3SiC_2 occurs when (111)TiC is parallel to 001(Ti_3SiC_2), therefore, there is an orientation relationship between TiC and Ti_3SiC_2 in the Ti–Si–C system [79,80]. Here, we observed similar orientation relationship between TiC and Ti_3SiC_2 grains. As illustrated in Fig. 21(f), (111)TiC is parallel to (001)Ti_3SiC_2 at the Ti_3SiC_2–TiC interface.

5. Conclusion

In this work, Ti_3SiC_2 was successfully fabricated in-situ by powder metallurgy spark plasma sintering using the MAX phase prealloyed starting powder. The reaction mechanism leading to the formation, decomposition and microstructural evolution of Ti_3SiC_2 was discussed, and the main conclusions are as follows:

1. The starting composition, carbon uptake and vacuum pressure during SPS plays a crucial role in high Ti_3SiC_2 conversion.
2. A starting powder mixture with excess silicon and deficient carbon

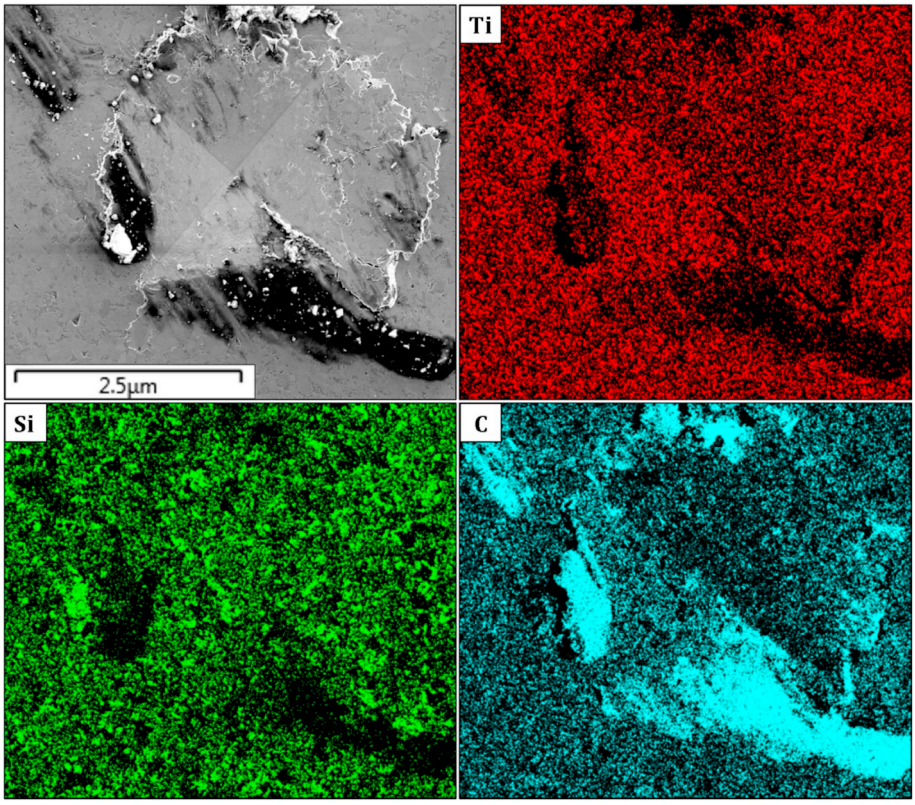

Fig. 17. EDS elemental map of the Vickers indentation print revealing evidence of amorphous carbon around the indent.

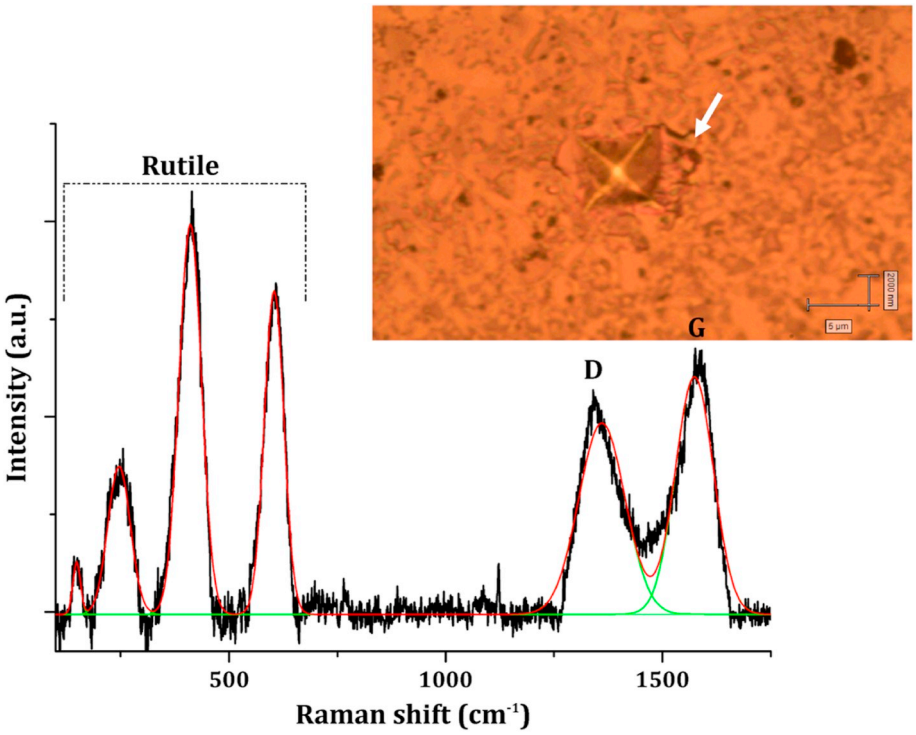

Fig. 18. Raman spectrum collected from the tribofilm region (white arrow) next to the indentation print revealing evidence of tribofilms (rutile (TiO_2) and D & G amorphous carbon Raman vibrational modes).

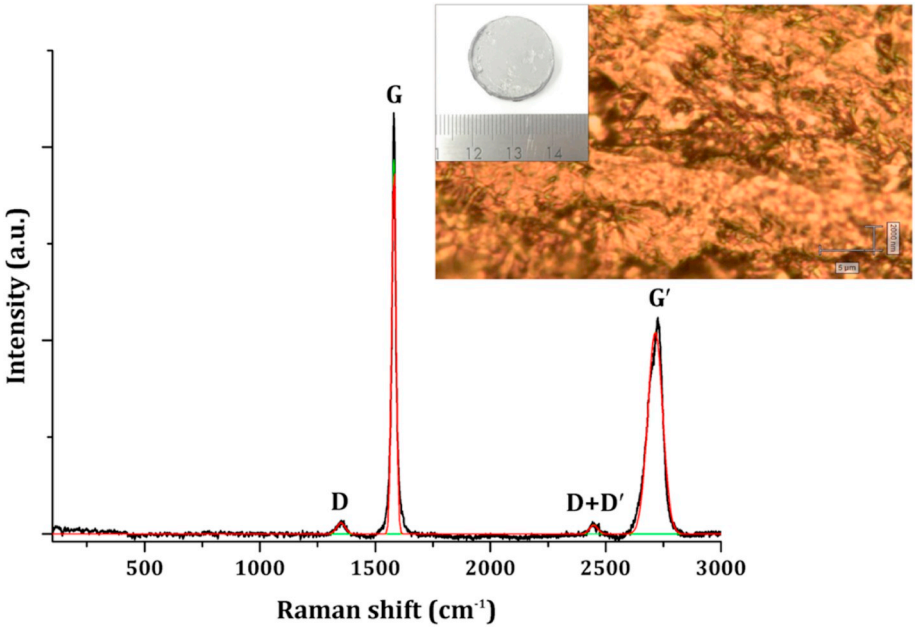

Fig. 19. Raman spectrum collected from the as-synthesized bulk sample surface after SPS. Inset shows the carburized surface where Raman spectrum was collected.

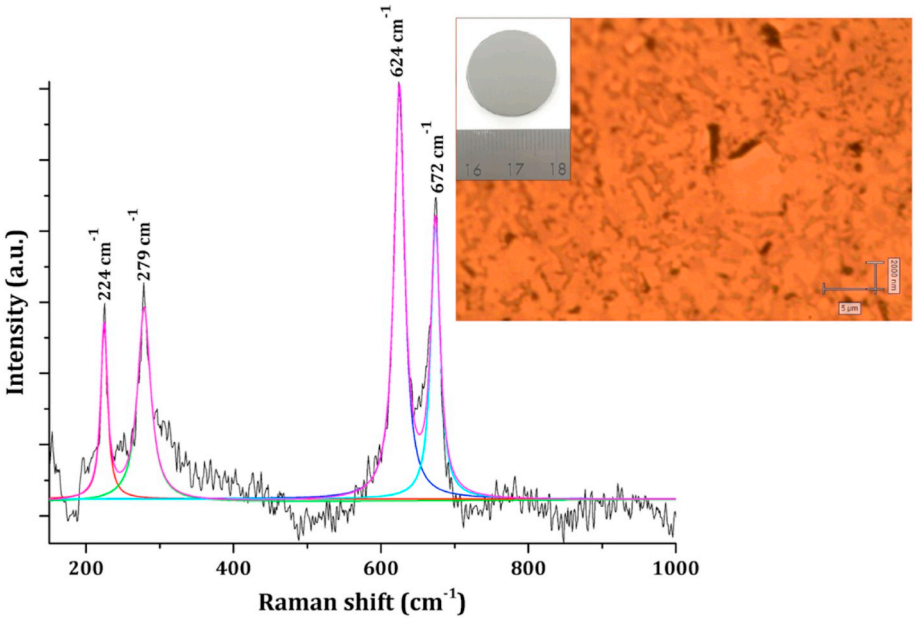

Fig. 20. Raman spectrum collected from the polished surface of the bulk sample. Inset shows the polished surface where the Raman spectrum was collected. Note stoichiometric TiC does not possess any Raman active modes.

(3Ti/(1 + x)Si/(1 - x)C) is needed to compensate for simultaneous Si-loss and carbon uptake, thus leading to high-purity Ti_3SiC_2. The use of boron nitride spray may further help mitigate against carburization from graphite paper.

3. Energy absorbing diffuse microcracking and deformation-induced micromechanisms via basal plane slip renders Ti_3SiC_2 tough and damage tolerant.
4. Ti_3SiC_2 is self-lubricating due to intrinsic rutile and amorphous carbon tribofilm formation.
5. The Maxthal 312 prealloyed starting powder route is suitable in the synthesis of Ti_3SiC_2 if purity of the bulk sample is not of interest such as in the synthesis of MAX phase composites. This is because Si-evaporation will push the overall bulk composition into a two-phase (Ti_3SiC_2–TiC) or three-phase (Ti_3SiC_2–$TiSi_2$–TiC) region with ancillary phases homogeneously distributed in the Ti_3SiC_2 matrix as they formed in-situ and not added as a second phase, thus a reinforcement the MAX phase compound is expected.

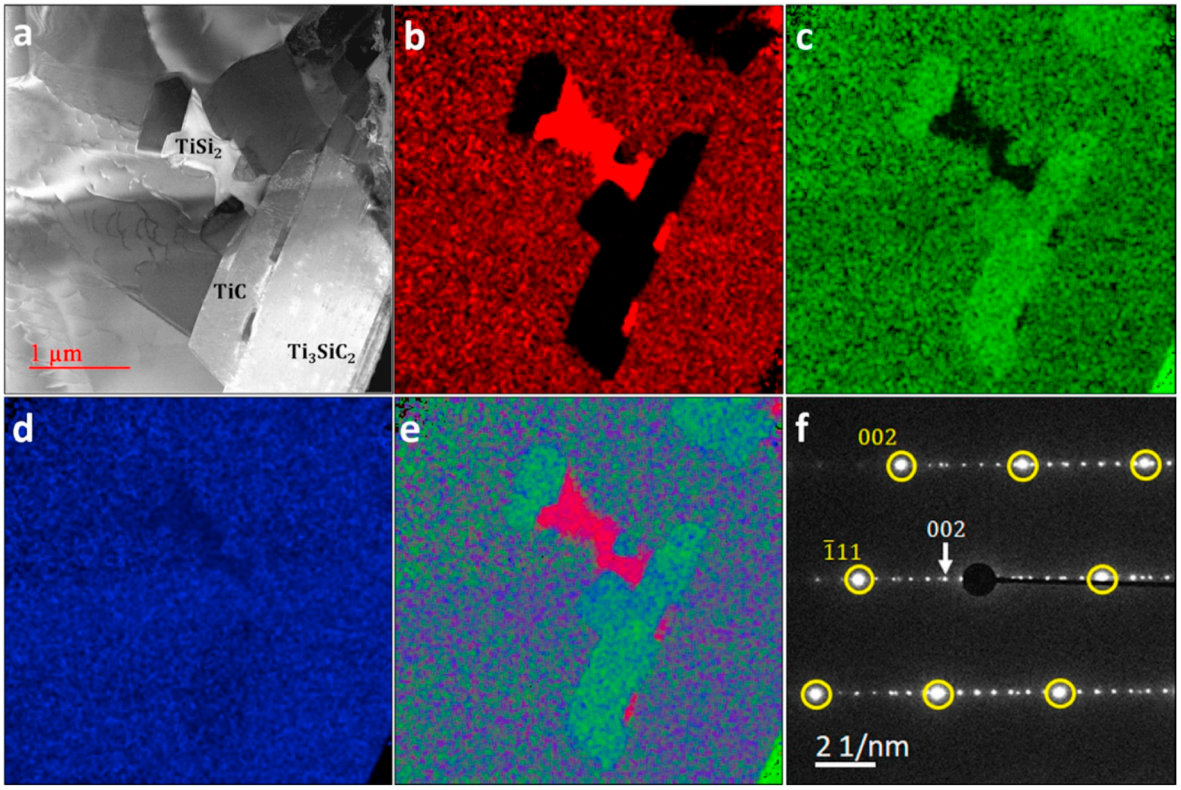

Fig. 21. (a) ADF STEM micrograph obtained from the bulk sample, (b) Si, (c) C and (d) Ti EDS elemental maps from (a). (e) Shows overlay maps of Ti, Si, and C. (f) SAD pattern obtained from the interface of TiC and Ti_3SiC_2 grains where [110]TiC and [100]Ti_3SiC_2 are parallel to the electron beam direction (SAD has been rotated ~ 22° counter-clockwise with regard to (a)). Diffraction spots associated to the TiC grain are highlighted using yellow circles. (For interpretation of the references to colour in this figure legend, the reader is referred to the Web version of this article.)

Declaration of competing interest

We declare no conflict of interest in this work.

References

[1] M. Sokol, et al., Big Questions in Chemistry - on the Chemical Diversity of the MAX Phases, (2019).
[2] H. Fashandi, et al., Synthesis of Ti3AuC2, Ti3Au2C2 and Ti3IrC2 by noble metal substitution reaction in Ti3SiC2 for high-temperature-stable Ohmic contacts to SiC, Nat. Mater. 16 (2017) 814.
[3] H. Fashandi, et al., Ti2Au2C and Ti3Au2C2 formed by solid state reaction of gold with Ti2AlC and Ti3AlC2, Chem. Commun. 53 (69) (2017) 9554–9557.
[4] M. Naguib, et al., Two-dimensional nanocrystals produced by exfoliation of Ti3AlC2, Adv. Mater. 23 (37) (2011) 4248–4253.
[5] B. Anasori, M.R. Lukatskaya, Y. Gogotsi, 2D metal carbides and nitrides (MXenes) for energy storage, Nature Reviews Materials 2 (2) (2017) 16098.
[6] M. Naguib, et al., Two-dimensional transition metal carbides, ACS Nano 6 (2) (2012) 1322–1331.
[7] J. Wang, et al., Discovery of hexagonal ternary phase Ti2InB2 and its evolution to layered boride TiB, Nat. Commun. 10 (1) (2019) 2284.
[8] M. Dahlqvist, B. Alling, J. Rosén, Stability trends of MAX phases from first principles, Phys. Rev. B 81 (2010) 220102.
[9] M.W. Barsoum, T. El-Raghy, The MAX Phases: unique New Carbide and Nitride Materials: ternary ceramics turn out to be surprisingly soft and machinable, yet also heat-tolerant, strong and lightweight, Am. Sci. 89 (4) (2001) 334–343.
[10] M.W. Barsoum, MAX Phases : Properties of Machinable Ternary Carbides and Nitrides, Wiley-VCH Verlag GmbH & Co. KGaA, Weinheim, Germany, 2013 2013.
[11] S. Hwang, et al., Machinability of Ti3SiC2 with layered structure synthesized by hot pressing mixture of TiCx and Si powder, J. Eur. Ceram. Soc. 32 (12) (2012) 3493–3500.
[12] T. El-Raghy, et al., Damage mechanisms around hardness indentations in Ti3SiC2, J. Am. Ceram. Soc. 80 (2) (1997) 513–516.
[13] B.J. Kooi, et al., Ti 3SiC 2: a damage tolerant ceramic studied with nano-indentations and transmission electron microscopy, Acta Mater. 51 (10) (2003) 2859–2872.
[14] I.M. Low, Vickers contact damage of micro-layered Ti3SiC2, J. Eur. Ceram. Soc. 18 (6) (1998) 709–713.
[15] D.J. Tallman, et al., Effect of neutron irradiation on select MAX phases, Acta Mater. 85 (2015) 132–143.
[16] Q. Huang, et al., Irradiation resistance of MAX phases Ti3SiC2 and Ti3AlC2: characterization and comparison, J. Nucl. Mater. 465 (2015) 640–647.
[17] C. Wang, et al., Irradiation-induced structural transitions in Ti2AlC, Acta Mater. 98 (2015) 197–205.
[18] J. Xiao, et al., Investigations on radiation tolerance of Mn + 1AXn phases: study of Ti3SiC2, Ti3AlC2, Cr2AlC, Cr2GeC, Ti2AlC, and Ti2AlN, J. Am. Ceram. Soc. 98 (4) (2015) 1323–1331.
[19] T. Lapauw, et al., Interaction of Mn + 1AXn phases with oxygen-poor, static and fast-flowing liquid lead-bismuth eutectic, J. Nucl. Mater. 520 (2019) 258–272.
[20] K. Lambrinou, T. Lapauw, A. Jianu, A. Weisenburger, J. Ejenstam, P. Szakálos, J. Vleugels, Corrosion-resistant ternary carbides for use in heavy liquid metal coolants, Ceram. Eng. Sci. Proc. 36 (7) (2016) 19–34.
[21] C. Magnus, J. Sharp, W.M. Rainforth, The lubricating properties of spark plasma sintered (SPS) Ti3SiC2 MAX phase compound and composite, Tribol. Trans. (2019) 1–14.
[22] S. Gupta, M.W. Barsoum, On the tribology of the MAX phases and their composites during dry sliding: a review, Wear 271 (9–10) (2011) 1878–1894.
[23] C. Magnus, et al., Microstructural evolution and wear mechanism of Ti3AlC2 – Ti2AlC dual MAX phase composite consolidated by spark plasma sintering (SPS), Wear 438–439 (2019) 203013.
[24] C. Magnus, W.M. Rainforth, Spark plasma sintering (SPS) synthesis and tribological behaviour of MAX phase composite of the family Tin + 1SiCn (n = 2), Wear 438–439 (2019) 203062.
[25] A. Crisan, O. Crisan, Low-temperature formation of 312 phase in Ti-Si-C ternary compound, Digest Journal of Nanomaterials and Biostructures 13 (2018) 155–162.
[26] J.M. Córdoba, et al., Synthesis of Ti3SiC2 powders: reaction mechanism, J. Am. Ceram. Soc. 90 (3) (2007) 825–830.
[27] Z.M. Sun, Progress in research and development on MAX phases: a family of layered ternary compounds, Int. Mater. Rev. 56 (3) (2011) 143–166.
[28] I.M. Low, W.K. Pang, Thermal stability of MAX phases, Key Eng. Mater. 617 (2014) 153–158.
[29] I.-M. Low, An overview of parameters controlling the decomposition and degradation of Ti-based M(n + 1)AX(n) phases, Materials 12 (3) (2019) 473.
[30] S.P. Munagala, MAX phases: new class of carbides and nitrides for aerospace structural applications, in: N.E. Prasad, R.J.H. Wanhill (Eds.), Aerospace Materials and Material Technologies : Volume 1: Aerospace Materials, Springer Singapore, Singapore, 2017, pp. 455–465.
[31] J. Zhang, et al., Microstructure and properties of Ti3SiC2/SiC nanocomposites fabricated by spark plasma sintering, Compos. Sci. Technol. 68 (2008) 499–505.
[32] J. Zhang, et al., Effect of TiC content on the microstructure and properties of Ti3SiC2–TiC composites in situ fabricated by spark plasma sintering, Materials Science and Engineering: A 487 (1–2) (2008) 137–143.
[33] N.V. Tzenov, M.W. Barsoum, Synthesis and characterization of Ti3AlC2, J. Am. Ceram. Soc. 83 (4) (2000) 825–832.
[34] K. Tang, et al., An X-ray diffraction study of the texture of Ti 3SiC 2 fabricated by hot pressing, J. Eur. Ceram. Soc. 21 (2001) 617–620.
[35] M.W. Barsoum, T. El-Raghy, Synthesis and characterization of a remarkable

ceramic: Ti3SiC2, J. Am. Ceram. Soc. 79 (7) (1996) 1953–1956.
[36] J. Zhang, et al., Fabrication of high purity Ti3SiC2 from Ti/Si/C with the aids of Al by spark plasma sintering, J. Alloys Compd. 437 (1–2) (2007) 203–207.
[37] W.B. Zhou, B.C. Mei, J.Q. Zhu, Fabrication of high-purity ternary carbide Ti3SiC2 by spark plasma sintering technique, Mater. Lett. 59 (12) (2005) 1547–1551.
[38] T. Lapauw, et al., A new method to texture dense Mn + 1AXn ceramics by spark plasma deformation, Scripta Mater. 111 (Supplement C) (2016) 98–101.
[39] N.C. Ghosh, S.P. Harimkar, K. Kalkan, R. Singh (Eds.), Synthesis and Tribological Characterization of In-Situ Spark Plasma Sintered Ti3SiC2 and Ti3SiC2-Tic Composites, 2012.
[40] M.A. El Saeed, F.A. Deorsola, R.M. Rashad, Optimization of the Ti3SiC2 MAX phase synthesis, Int. J. Refract. Metals Hard Mater. 35 (2012) 127–131.
[41] V. Gauthier, et al., Self-propagating high-temperature synthesis of Ti3SiC2: study of the reaction mechanisms by time-resolved X-ray diffraction and infrared thermography, J. Am. Ceram. Soc. 89 (2006) 2899–2907.
[42] F. Meng, B. Liang, M. Wang, Investigation of formation mechanism of Ti3SiC2 by self-propagating high-temperature synthesis, Int. J. Refract. Metals Hard Mater. 41 (2013) 152–161.
[43] Y. Khoptiar, I. Gotman, Synthesis of dense Ti3SiC2-based ceramics by thermal explosion under pressure, J. Eur. Ceram. Soc. 23 (1) (2003) 47–53.
[44] W.K. Pang, et al., 15 - phase and thermal stability in Ti3SiC2 and Ti3SiC2/TiC/TiSi2 systems, Advances in Science and Technology of Mn + 1axn Phases, Woodhead Publishing, 2012, pp. 389–413.
[45] Z.F. Zhang, et al., Application of pulse discharge sintering (PDS) technique to rapid synthesis of Ti3SiC2 from Ti/Si/C powders, J. Eur. Ceram. Soc. 22 (16) (2002) 2957–2961.
[46] B. Xu, et al., Synthesis of single-phase Ti3SiC2 from coarse elemental powders and the effects of excess Al, Ceram. Int. 45 (1) (2019) 948–953.
[47] H. Foratirad, H. Baharvandi, M.G. Maraghe, Effect of excess silicon content on the formation of nano-layered Ti3SiC2 ceramic via infiltration of TiC preforms, J. Eur. Ceram. Soc. 37 (2) (2017) 451–457.
[48] C. Qin, et al., Microstructure characterization and mechanical properties of TiSi2-SiC-Ti3SiC2 composites prepared by spark plasma sintering, 47 (2006) 845–848.
[49] I. Kero, R. Tegman, M.-L. Antti, Phase reactions associated with the formation of Ti3SiC2 from TiC/Si powders, Ceram. Int. 37 (7) (2011) 2615–2619.
[50] X. Wang, Y. Zhou, Solid-liquid reaction synthesis and simultaneous densification of polycrystalline Ti 2 AlC, Zeitschrift fuer Metallkunde/Materials Research and Advanced Techniques 93 (2002) 66–71.
[51] X. Wang, Y. Zhou, Solid–liquid reaction synthesis of layered machinable Ti3AlC2 ceramic, J. Mater. Chem. 12 (3) (2002) 455–460.
[52] A. Guitton, et al., Evidence of dislocation cross-slip in MAX phase deformed at high temperature, Sci. Rep. 4 (2014) 6358-6358.
[53] L. Farber, et al., Dislocations and stacking faults in Ti3SiC2, J. Am. Ceram. Soc. 81 (2005) 1677–1681.
[54] X.H. Wang, Y.C. Zhou, Oxidation behavior of Ti3AlC2 powders in flowing air, J. Mater. Chem. 12 (9) (2002) 2781–2785.
[55] F. Sato, J. Li, R. Watanabe, Reaction Synthesis of Ti3SiC2 from Mixture of Elemental Powders vol. 41, (2000), pp. 605–608.
[56] Z.-F. Zhang, et al., A new synthesis reaction of Ti3SiC2 from Ti/TiSi2/TiC powder mixtures through pulse discharge sintering (PDS) technique, Material Research Innovations 5 (3) (2002) 185–189.
[57] I. Kero, M.-L. Antti, M. Odén, Synthesis of Ti3SiC2 by Reaction of TiC and Si Powders, (2009), pp. 21–30.
[58] H. Li, et al., Synthesis of Ti3SiC2 by pressureless sintering of the elemental powders in vacuum, Mater. Lett. 58 (11) (2004) 1741–1744.
[59] J.T. Li, Y. Miyamoto, Fabrication of monolithic Ti3SiC2 ceramic through reactive sintering of Ti/Si/2TiC, J. Mater. Synth. Process. 7 (2) (1999) 91–96.
[60] C. Racault, F. Langlais, R. Naslain, Solid-state synthesis and characterization of the ternary phase Ti3SiC2, J. Mater. Sci. 29 (13) (1994) 3384–3392.
[61] A. Pourebrahim, et al., Low temperature synthesis of high-purity Ti3SiC2 via additional Si through spark plasma sintering, J. Alloys Compd. 789 (2019) 313–322.
[62] M.J. Abu, J.J. Mohamed, Z.A. Ahmad, Effect of excess silicon on the formation of Ti3SiC2 using free Ti/Si/C powders synthesized via arc melting, ISRN Ceramics (2012) 10 2012.
[63] Z.F. Zhang, et al., Effects of sintering temperature and Si content on the purity of Ti3SiC2 synthesized from Ti/Si/TiC powders, J. Alloys Compd. 352 (1) (2003) 283–289.
[64] A. Pourebrahim, et al., Effect of aluminum addition on the densification behavior and mechanical properties of synthesized high-purity nano-laminated Ti3SiC2 through spark plasma sintering, J. Alloys Compd. 730 (2018) 408–416.
[65] Y. Zou, et al., Effect of Al addition on low-temperature synthesis of Ti3SiC2 powder, J. Alloys Compd. 461 (1–2) (2008) 579–584.
[66] Z. Jiaoqun, M. Bingchu, Effect of aluminum on synthesis of Ti3SiC2 by spark plasma sintering (SPS) from elemental powders, J. Mater. Synth. Process. 10 (6) (2002) 353–358.
[67] J.O. Zhu, et al., Effect of aluminum on the reaction synthesis of ternary carbide Ti3SiC2, Scripta Mater. 49 (7) (2003) 693–697.
[68] T. El-Raghy, M.W. Barsoum, Diffusion kinetics of the carburization and silicidation of Ti3SiC2, J. Appl. Phys. 83 (1) (1998) 112–119.
[69] Z.F. Zhang, et al., Micron-scale deformation and damage mechanisms of Ti3SiC2 crystals induced by indentation, Adv. Eng. Mater. 6 (12) (2004) 980–983.
[70] A. Murugaiah, et al., Spherical nanoindentations and kink bands in Ti3SiC2, J. Mater. Res. 19 (4) (2011) 1139–1148.
[71] S.B. Li, J.X. Xie, L.T. Zhang, L.F. Cheng, Synthesis and some properties of Ti3SiC2 by hot pressing of Ti, Si and C powders Part 2 – mechanical and other properties of Ti3SiC2, Mater. Sci. Technol. 21 (9) (2005) 1054–1058.
[72] M. Barsoum, M. Radovic, Mechanical Properties of the MAX Phases vol. 41, (2011), pp. 195–227.
[73] M.W. Barsoum, L. Farber, T. El-Raghy, Dislocations, kink bands, and room-temperature plasticity of Ti3SiC2, Metall. Mater. Trans. 30 (7) (1999) 1727–1738.
[74] F. Tuinstra, J.L. Koenig, Raman spectrum of graphite, J. Chem. Phys. 53 (3) (1970) 1126–1130.
[75] S. Santangelo, et al., Evaluation of crystalline perfection degree of multi-walled carbon nanotubes: correlations between thermal kinetic analysis and micro-Raman spectroscopy, J. Raman Spectrosc. 42 (4) (2011) 593–602.
[76] S. Challagulla, et al., Structure sensitive photocatalytic reduction of nitroarenes over TiO_2, Sci. Rep. 7 (2017).
[77] M. Amer, et al., The Raman spectrum of Ti3SiC2, J. Appl. Phys. 84 (10) (1998) 5817–5819.
[78] A. Dmitruk, et al., Development of pore-free Ti-Si-C MAX/Al-Si composite materials manufactured by squeeze casting infiltration, J. Mater. Eng. Perform. 28 (2019) 6248–6257.
[79] K. Tang, et al., A study on the orientation relationship between Ti3SiC2 and TiC grains, Mater. Lett. 57 (1) (2002) 106–109.
[80] Z.J. Lin, et al., Microstructural relationship between compounds in the Ti–Si–C system, Scripta Mater. 55 (2006) 445–448.